J. Electrochem. Sci. Eng. **13(4)** (2023) 641-658; http://dx.doi.org/10.5599/jese.1655

Open Access : : ISSN 1847-9286
https://pub.iapchem.org/ojs/index.php/JESE

Original scientific paper

Impact of carbon coating processing using sucrose for thick binder-free titanium niobium oxide lithium-ion battery anode

Chen Cai, Patrick McCormack, Ziyang Nie, Gary M. Koenig Jr.✉

Department of Chemical Engineering, University of Virginia, 102 Engineers Way, Charlottesville, 22904-4741, VA, USA

Corresponding author: ✉*gary.koenig@virginia.edu; Tel.: +1-434-982-2714; Fax: +1-434-982-2658*

Received: December 30, 2022; Accepted: May 4, 2023; Published: May 21, 2023

Abstract

Lithium-ion batteries are increasingly important for providing energy storage solutions. In the drive to improve the energy density at the cell level, optimizing the electrode architecture is crucial in addition to researching new materials. Binder-free (BF) electrodes include porous pellets only containing battery electroactive materials. These electrodes can provide advantages with regard to mechanical stability and alleviated ion transport limitations relative to composite approaches for very thick and energy-dense electrodes. However, the absence of conductive additives often limits suitable material candidates for BF battery electrodes. $TiNb_2O_7$ *(TNO) is a promising BF electrode material from a gravimetric and volumetric capacity standpoint, but phase pure TNO has relatively low electronic conductivity. Herein, a sucrose precursor coating method for TNO materials was implemented to process the TNO materials into BF electrodes. The sucrose served as a source to generate carbon in the electrodes, where the carbon coating resulted in an increase in rate capability, discharge voltage, and cycle life.*

Keywords

Electronic conductivity; mechanical stability; rate capability; discharge voltage; cycle life

Introduction

Stimulated by rapid improvements in portable electronics energy storage solutions, batteries have drawn extensive attention. Lithium-ion (Li-ion) batteries have dominated the portable electronics market for years [1,2]. Towards further improvements in Li-ion battery energy and power density, efforts have been directed towards both new materials and electrode architecture improvements [3,4]. Increasing electrode thickness is a straightforward route to improve cell-level energy density; however, with conventional composite electrodes, increased thickness results in very restricted ion transport, limiting power density and rate capability [5-9]. Delamination for composite electrodes from the current collector at increasing thickness is also a consideration [10,11]. Several approaches have been investigated to mitigate ionic transport limitations originating from the polymer binder and conductive additives which occupy the interstitial microstructure in conventional composite electrodes [12-14]. An alternative electrode architecture to mitigate some of the challenges of processing/cycling thick electrodes is binder-free electrodes (referred to as BF electrodes in this paper, and also “sintered electrodes”, or “all active material (AAM) electrodes” in some prior works with similar processing), which is composed of only electroactive material and electrolyte-laden pores/voids [15-17]. BF electrodes are mechanically strengthened using a mild sintering treatment after hydraulic compression of the electroactive material powder [18-25]. These electrodes have reported thicknesses well over a half millimeter and areal loadings exceeding 150 mg cm^{-2} [18-24].

In the absence of conductive additives, electron transport through the electrode matrix must occur via the electroactive material itself rather than a percolated network of conductive carbon [18]. Prior research has shown that when the electronic conductivity of the electrode matrix is greater than 1 S m^{-1}, it no longer limits the electrochemical cell performance for typical Li-ion electrolyte ion transport properties [8]. In a previous report from our group, BF full cells using $LiCoO_2$ (LCO) as cathode and $Li_4Ti_5O_{12}$ (LTO) as anode were successfully charged/discharged over many cycles [19]. Although before cycling, the electronic conductivity of the materials in the LTO/LCO cell can be as low as 10^{-5} S m^{-1}, over 95 % of the lithiation range of the electroactive materials during cycling have electronic conductivities exceeding 10 S m^{-1}, an electronic conductivity magnitude where the electrochemical charge/discharge rate would be expected to be limited by ionic transport limitations over electronic transport resistances [20-22,26-28]. Despite the excellent electronic conductivity and stability of LTO, the volumetric and gravimetric energy densities are still relatively low [22,29]. An important note here is that the very common carbon-based Li-ion anodes, such as graphite, cannot be used in the BF electrode architecture. This is because (i) at such high loading, even at relatively low C-rate high areal current density results, which readily induces lithium plating [30]; (ii) the ~13 % lattice volume change is too great to be accommodated in BF electrodes without the addition of elastic polymer [31]; and (iii) with increased thickness, the solid electrolyte interface (SEI) formation can clog pores, exacerbating ion transport restrictions [32]. To improve the energy density, an alternative anode material, $TiNb_2O_7$ (TNO), will be investigated herein. TNO has relatively high gravimetric and volumetric capacity but relatively low electronic conductivity (especially relative to LTO), which was expected to be a challenge to implement TNO within the BF electrode architecture. TNO does have an increasing electronic conductivity with lithiation of the material [33-38]; however, the increase has still been reported to be well below the ionic conductivity of typical Li-ion electrolytes [39], suggesting that matrix electronic conductivity would still be expected to limit the electrochemical outcomes of cells with TNO electrodes.

There are different strategies to improve or overcome the inherent electronic conductivity limitations of electroactive materials. One route is to dope the electroactive material with elements that result in increased electronic conductivity, and this method has even been applied to BF electrodes, an example being the material $LiMn_2O_4$ (LMO) [18]. There are limits to the electronic conductivity improvements via doping methods, and secondary phases can result in too high of a doping level [40,41]. Another option is to coat the electroactive material with metal oxides, carbon, and other materials, and this strategy has been attributed to improving the rate capability of low electronic conductivity electroactive materials such as olivine-phase $LiFePO_4$ and layered-phase $LiNi_{0.6}Co_{0.2}Mn_{0.2}O_2$ [42-44]. Among coatings, carbon-based coating of electroactive materials has been broadly reported for improved interfacial stability and electronic conductivity [42,45-50]. Sucrose is a common carbon source that also can serve as a particle binder material [46,51]. Herein, we propose a facile method to fabricate carbon-coated BF electrodes using sucrose both as a sacrificial binder necessary for BF electrode processing and as a carbon source, where the carbon coating process does not require an extra step for treating the electroactive material powder or the BF porous pellet relative to processing the electrodes without the coating.

The carbon coating processing targeted in this report has a schematic illustration in Figure 1. The electroactive material, TNO, was initially synthesized via a sol-gel route. The TNO powder was then coated with sucrose via mixing with an aqueous solution containing dissolved sucrose and drying of the solvent. The sucrose-coated powder was hydraulically pressed into a porous pellet. Finally, the pellet was heated in an inert atmosphere which converted the sucrose to carbon and resulted in a porous BF pellet of TNO with remaining residual carbon from the sucrose source.

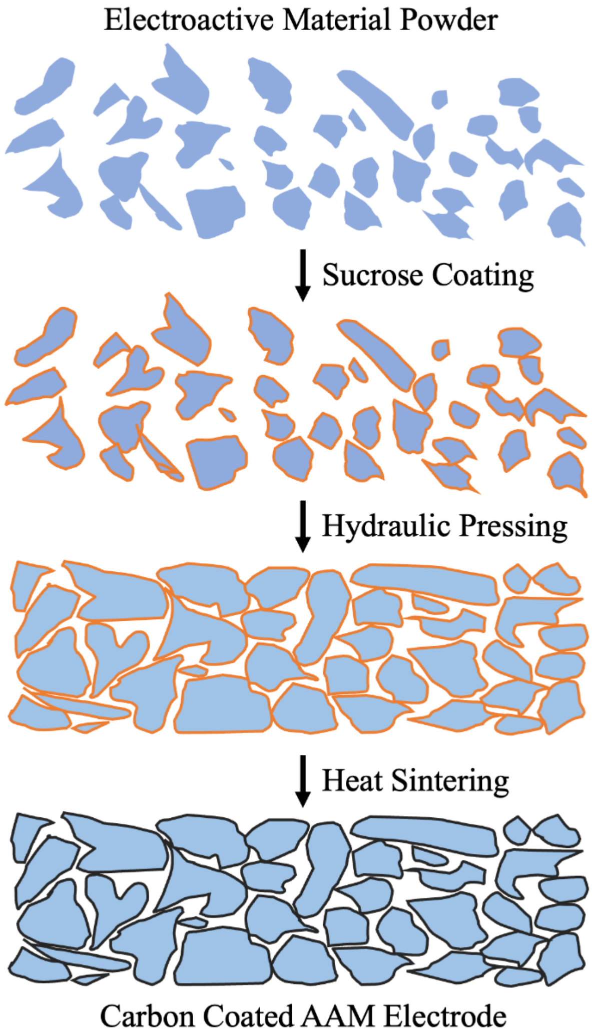

Figure 1. *Schematic of the process for fabricating carbon-coated BF TNO electrodes*

Experimental

Electroactive material powder synthesis

TNO electroactive material powder was synthesized using a sol-gel method. Briefly, 0.5 M of niobium chloride ($NbCl_5$, Sigma-Aldrich) and 0.25 M of titanium isopropoxide ($Ti(OC_3H_7)_4$, Sigma-Aldrich) were dissolved in 40 mL ethanol at 40 °C and stirred at 300 RPM to facilitate dissolution and mixing. The solution was dried at room temperature overnight in air, then redissolved in 40 mL deionized (DI) water and dried at 80 °C overnight in air within a fume hood. The resulting precursor was then heated to 700 °C and held at that temperature for 2 hours, where the ramp rates for heating and cooling were both 1 °C min^{-1}.

LCO electroactive material powder was synthesized via precipitation of a precursor followed by a solid-state reaction [25]. 0.2 M of cobalt sulfate heptahydrate ($CoSO_4 \times 7H_2O$, Acros Organics) and 0.2 M of sodium oxalate ($Na_2C_2O_4$, Fisher) were separately dissolved into 400 mL of DI water each and heated to 60 °C. The solutions were mixed via pouring all at once, and the mixture was stirred at 300 RPM. The reaction was allowed to proceed for 30 min before collection of the precipitate via vacuum filtration. The filter cake was rinsed with 1.6 L of DI water. The resulting powder cake was dried at 80 °C overnight in air and blended with lithium carbonate (Li_2CO_3, Fisher Chemical) with a molar ratio of 1.05:1 Li:Co using a mortar and a pestle by hand for 10 min. The blended powder was then heated at a ramp rate of 1 °C min^{-1} to 800 °C without a hold at the top temperature and then allowed to cool to room temperature without control over the cooling rate.

Material characterization

Thermogravimetric analysis (TGA) was conducted using a TA Instruments Q50. Heating initiated from room temperature to 800 °C at a ramp rate of 10 °C min^{-1} in air atmosphere. Scanning electron micrographs (SEMs) were collected using a FEI Quantum 650. Powder X-ray diffraction (XRD) was conducted using a PANalytical X'pert ProMPD.

The electronic conductivity of materials was measured using a direct current (DC) technique. The as-prepared BF pellet electrodes were coated with silver paste (Sigma-Aldrich) by hand on each flat side of the porous disc. The coated pellets were sandwiched between stainless steel and compressed by a clamp. A constant voltage at 10 mV was applied and the current was recorded using a Gamry Reference 600 to measure the DC resistance necessary to calculate the pellet material's electronic conductivity.

BF electrode fabrication

During the fabrication of BF TNO electrodes, 4 concentrations of sucrose binder were prepared in this work. The sucrose contents were 0.0, 2.5, 5.0, and 7.5 % by mass (denoted by 0.0 , 2.5, 5.0 and 7.5 % sucrose). The content indicates the mass percent of sucrose relative to the total combined mass of sucrose and TNO. For the 0.0 % sucrose sample, 1 g of TNO powder was blended with 2 mL of 1 wt.% polyvinyl butyral (PVB) solution (Pfaltz & Bauer) in ethanol using a mortar and pestle by hand until dry. For the other three samples containing sucrose, a total mass of 1 g consisting of TNO and sucrose powder was blended with 0.5 mL of DI water and 1.5 mL of ethanol using a mortar and a pestle by hand until dry. For all cases, the coated powder was next loaded into a circular pellet die (Carver) with a diameter of 1.3 cm, followed by pressing at 420 MPa for 2 min using a hydraulic press (Carver). The pressed pellet was sintered in an argon atmosphere at 800 °C for 1 hour at ramp-up and down rates of 2 °C min^{-1}. The as-prepared pellets had thicknesses ranging between 580 and 610 µm (measured using digital calipers), areal loadings of 142-148 mg cm^{-2}, and geometric pore/void fraction of 0.43-0.45 (calculated assuming the crystal density to be 4.3 g cm^{-3}) [52]. In addition, thinner BF electrodes were fabricated to facilitate cycle life testing, with loadings of 18 to 20 mg cm^{-2} and thicknesses ranging between 70 and 80 µm. Note that carbon-coated (and carbon-free) TNO powders were also used in composite electrodes, and for TNO powders used for composite electrodes, all processing steps were the same as for BF electrodes except that there was no hydraulic compression of the powder.

For BF LCO electrodes, 1 g of LCO powder was blended with 2 mL of 1 wt.% PVB solution in ethanol using a mortar and a pestle by hand until dry. The pressing procedure was the same as above for TNO materials. The pressed pellet was sintered in air at 600 °C for 1 hour at both ramp-up and down rates of 1 °C min^{-1}. The as-prepared pellets had measured thicknesses ranging between

810 and 850 μm, areal loadings of 268 to 273 mg cm^{-2}, and geometric pore/void fractions of 0.32 to 0.34 (calculated assuming the crystal density to be 5.0 g cm^{-3}) [22]. Thinner BF LCO electrodes were also fabricated to facilitate cycle life testing at 37 to 38 mg cm^{-2}, with thicknesses of ∼120 μm. Detailed characterization of BF LCO electrodes can be found elsewhere for materials fabricated using the same procedures [19-21].

Electrochemical evaluation

For composite electrode cells, the TNO powder was mixed with acetylene carbon black (CB, Alfa Aesar) and 3.33 wt.% polyvinyl pyrrolidone (PVP, Sigma Aldrich, 360 kDa molecular weight) in ethanol solution with a mass ratio TNO:PVP:CB of 8:1:1. The resulting slurry was coated onto an aluminum foil current collector using a doctor blade, which resulted in final areal active material loadings measured for punched electrodes to range between 2.0-3.5 mg cm^{-2} after drying. Circular electrodes with an area of 1.33 cm^2 were punched by hand using a die and transferred into a glove box filled with argon. Punched lithium metal foil was used as anodes and Celgard 2325 was the separator, and the electrodes were assembled into electrochemical cells using 2032-type coin cell parts, with assembly all in the glove box. The electrolyte was 1.2 M $LiPF_6$ in 3:7 ethylene carbonate:ethyl methyl carbonate (Gotion). The as-prepared cells were evaluated using a multichannel battery cycler (MACCOR) between 1.0-2.5 V at C/20, where 387.6 mAh g^{-1} was assumed to be the TNO theoretical capacity used for adjusting the currents for the C rate determination [46]. For Li/TNO cells, cycling starts on a discharge.

For BF electrode cells, the as-prepared BF cathode (LCO pellet) and BF anode (TNO pellet) were attached to the bottom plate and the spacer of the 2032-type coin cell, respectively, with a custom carbon paste applied between the BF electrode and stainless steel to reduce contact resistance. The custom carbon paste was applied as a homogenous slurry consisting of 4.76 wt.% of CB, 4.76 wt.% of PVP, and 90.48 wt.% of ethanol. Pellets adhered to the cell components with the paste were then dried in a vacuum at 80 °C for 20 min before transferring into the glove box. It is noted that the carbon paste amount was less than 1 mg cm^{-2}, which was <1 % of the mass of the thicker BF electrodes. 2032-type coin cells were assembled with a single spacer attached to the anode, as the cathode was directly attached to the bottom piece. The same electrolyte was used for the composite electrodes described above. Glass fiber (Fisher, type G6 circles) was used as a separator. Although glass fiber has a relatively large thickness compared to porous polymer options, this separator was used to minimize the possibility of a short between the relatively rough ceramic surfaces of the pellets. While not quantitatively confirmed or estimated, the glass fiber would be expected to compress during cell assembly resulting in a lower thickness. The compression on porous polymer separators has been previously speculated to increase ion transport limitations in similarly constructed cells [23]. The BF cells were cycled between 1.0-3.2 V, and as a reference point for C rates, 1.69 mA cm^{-2} corresponded to a rate of C/20.

For thinner BF electrode cells, the cells were cycled between 1.0 and 3.2 V at 2 mA cm^{-2} (∼C/2) for 100 cycles. Electrochemical impedance spectroscopy (EIS) was conducted on the cycled cell using a Gamry Reference 600.

Results and discussion

Electrochemical evaluation

The initial sol-gel synthesized powder with the targeted TNO composition had broad peaks in collected XRD patterns, suggesting relatively low crystallinity. The XRD and relevant reference patterns for titanium niobate phases can be found in Supplementary material, Figure S-1. The broad peaks may have partly been due to the relatively low calcination temperature and were consistent with previous reports [53-55]. Explicit assignment of each individual peak was challenging to affirm unambiguously; however, there were $Ti_xNb_yO_z$ phases that could be associated with all peaks [56,57]. SEM images of the initial sol-gel synthesized powder can be found in Supplementary material, Figure S-2. These micrographs suggested the morphology of the material was secondary aggregates that had length dimensions of approximately 20 µm, while the primary particles that formed the larger aggregates were less than 1 µm in length (with many primary particles in the size range of ~100 nm).

Figure 2a shows the estimated mass percentage of carbon on the TNO materials with the different amounts of sucrose added before hydraulic compression and thermal treatment in an inert atmosphere.

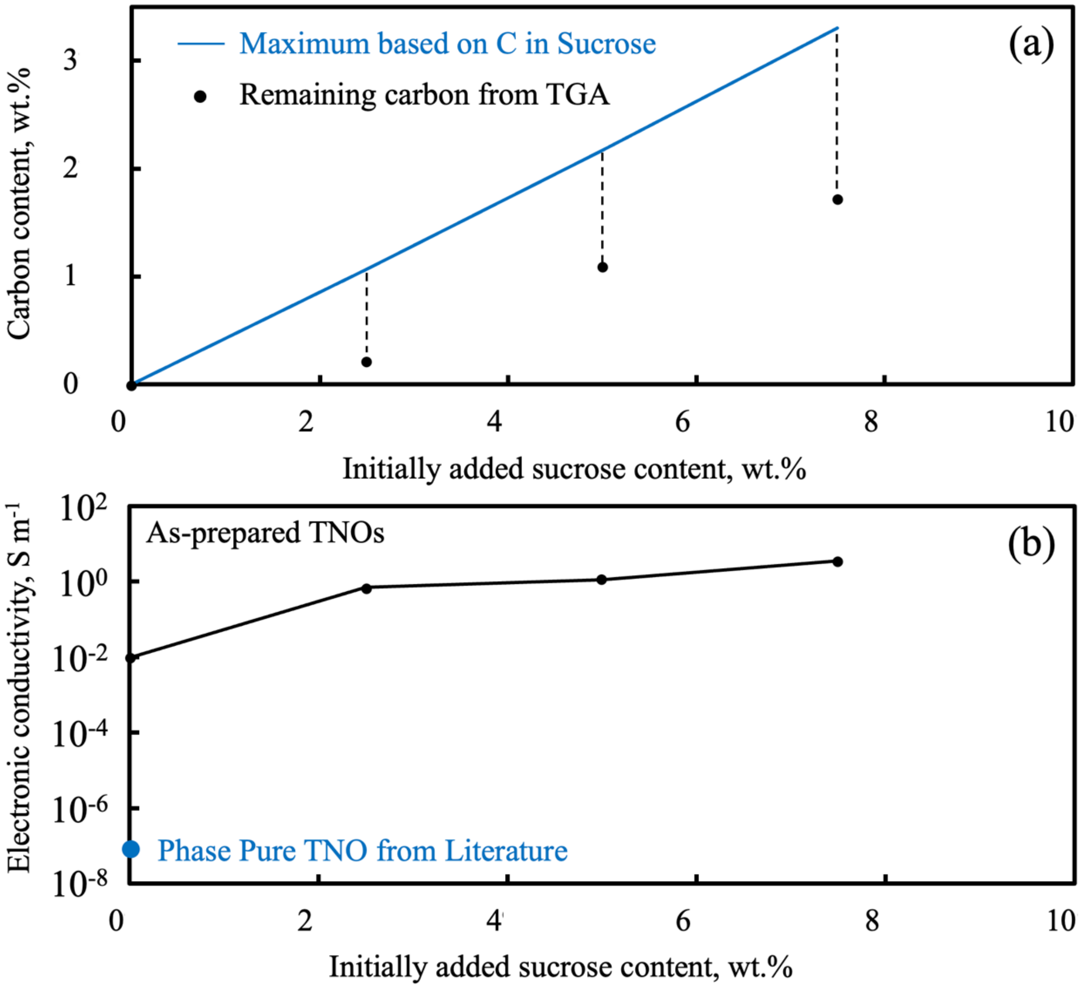

Figure 2. *(a) Theoretical maximum carbon content (blue line) and actual (black dots) carbon content determined from TGA for different initial added sucrose content to the TNO material before thermal treatment. (b) Electronic conductivities of as-prepared pellet (black) and phase pure literature value (blue)* [33]

The measured carbon mass percentage was estimated from the mass change during TGA experiments at 800 °C relative to room temperature, and the more detailed TGA data can be found in Supplementary material, Figure S-3. Carbon loss/oxidation was observed to occur between 400 and 500 °C, consistent with previous reports [54,58]. As the sucrose content added to the powder increased, the relative mass content of the carbon coating increased as well. An additional note is that based on the elemental C content of sucrose, theoretically, for the mass of sucrose, if all that C was converted to a carbon coating 42 wt.% of the initial sucrose mass would be expected to remain. The blue line in Figure 2a depicts the amount of carbon expected if all the C in the sucrose was converted to a carbon coating. As can be seen, the carbon content for all samples was below these theoretical values, suggesting loss of carbon to other processes, such as reduction of the TNO material at the interface. It is also noted that the difference between the theoretical maximum carbon and carbon determined from TGA increased as the sucrose added increased, suggesting less efficiency of sucrose conversion to a carbon coating as the sucrose content was increased.

The DC electronic conductivity measured using TNO porous pellets can be seen in Figure 2b. All TNO materials exhibited higher electronic conductivity than reported for phase pure $TiNb_2O_7$ from the literature [33]. Even with the 0.0 % sucrose sample, the conductivity was ~5 orders of magnitude higher, and this higher conductivity was suspected to result in part from the presence of the $TiNbO_4$ phase (consistent with XRD results discussed in the next paragraph), which has a much higher electronic conductivity reported at ~150 S m^{-1} [59]. Additionally, there may have been some reduction of the $TiNb_2O_7$ phase, which can have a large impact on the electronic conductivity of this material [33]. For the materials processed with sucrose and subsequently coated with carbon, the electronic conductivity also increased as the carbon coating content increased. The final measured conductivities for the materials with the highest carbon content were over 1 S m^{-1}.

XRD patterns for the TNO pellets after hydraulic compression and heating in an argon atmosphere can be found in Figure 3. All four amounts of sucrose addition resulted in similar XRD patterns. The major phase was assigned as $TiNb_2O_7$, a monoclinic layered structure with a space group of C2/m [46]. An impurity phase was also noted after thermal treatment, attributed to $TiNbO_4$, suggesting a partial reduction of some Nb^{5+} to Nb^{4+} in the pellet [59-61]. The peaks consistent with arising due to a $TiNbO_4$ impurity are marked in Figure 3. It is noted that to the naked eye, visually, the 0.0 % sucrose exhibited dark blue color, while the carbon-coated samples were all dark grey, consistent with previous literature [61].

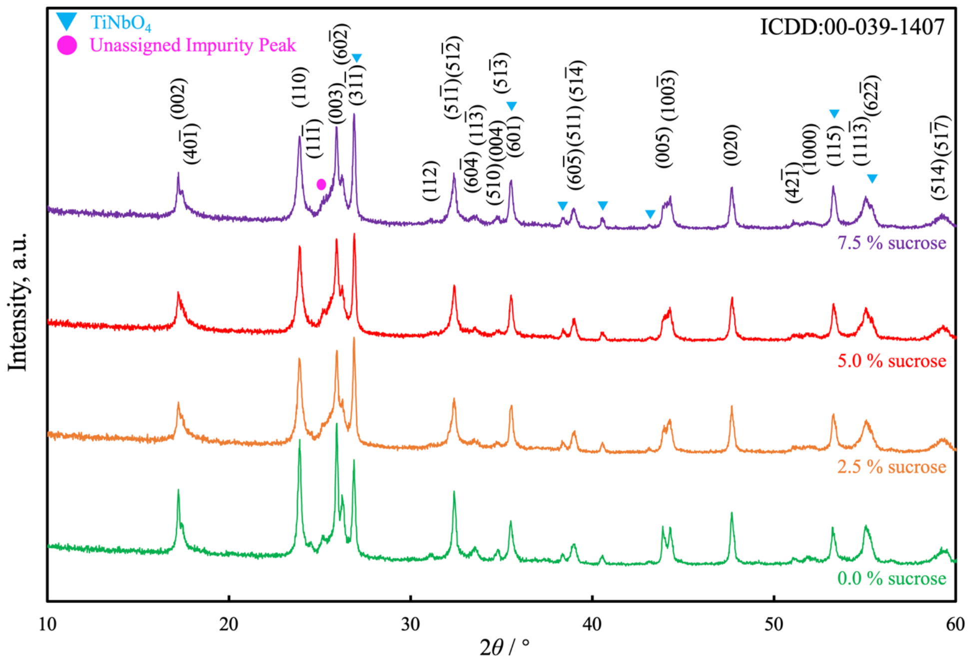

Figure 3. *XRD patterns for 0.0 (green), 2.5 (orange), 5.0 (red) and 7.5 % sucrose (purple)*

There was an additional small impurity peak at a 2θ position of ~25°. Explicit assignment of this peak was difficult, although likely candidates could be other Nb-enriched oxide phases such as $TiNb_{24}O_{62}$, $Ti_2Nb_{14}O_{39}$, and $Ti_2Nb_{10}O_{29}$ based on bulk stoichiometry [57,62-64]. Since the bulk molar ratio of Ti:Nb from sol-gel synthesis was 1:2, the presence of $TiNbO_4$ suggested the presence of one or multiple of these Nb-enriched phases.

SEM images of the 0.0, 2.5, 5.0 and 7.5 % sucrose can be found in Supplementary material, Figure S-4. All samples had a similar appearance. Many of the primary particle sizes were still on the order of ~100 nm, as was the case for the powder before hydraulic compression and thermal treatment. The retention of the primary particle size was also consistent with the mild sintering process. These primary particles were part of larger aggregates 10-20 µm in size. Many of the aggregates appeared flattened, which likely resulted from the hydraulic compression processing step.

Electrochemical evaluation

Initial electrochemical analysis on the TNO materials was conducted using composite electrodes paired with Li metal anodes. The first charge and discharge cycles of all materials in composite half cells paired with Li anodes can be found in Supplementary material, Figure S-5. As the sucrose content added to the TNO before heat treatment increased, the gravimetric capacity of the resulting TNO electroactive material decreased. The decrease in gravimetric capacity was likely due to increasing inactive carbon content in the powder and increasing relative amounts of $TiNbO_4$ phase. The voltage where $TiNbO_4$ has electrochemical capacity is between 1.0 and 2.0 V and thus overlaps with TNO; however, $TiNbO_4$ has a reported capacity of 200 mAh g^{-1} and thus increase in its content would lower the overall material gravimetric capacity relative to TNO [60].

Next, electrochemical characterization was done of cells containing the TNO BF electrodes directly. The TNO materials were used as BF anodes paired with LCO BF cathodes in a full-cell configuration. BF electrodes were not evaluated in half cells due to the limitations of using lithium metal in such high areal capacity systems, where each cycle would have a significant amount of plating and stripping that make the Li electrode the limiting factor [19]. As for BF cells paired with LCO, when looking at the discharge voltage profiles (Figure 4), at a relatively slow rate of C/20, the 0.0 % sucrose had the largest capacity as expected because at low rates the resistance due to that material having the lowest matrix electronic conductivity did not impact the electrochemical capacity. At higher rates of C/10 and C/5, the 2.5 % sucrose had the highest capacity among all materials evaluated. This outcome was not explained simply by improvements in the electronic conductivity of the electrode matrix. For such a thick BF electrode, the cell would be expected to be limited by ion transport through the electrolyte-laden electrode microstructure at such rates due to Li depletion in the cathode region [20,22]. As the sucrose content increased, the voltage decreased with a steeper slope near the later discharge region (*e.g.*,>150 mAh g^{-1} anode) at both C/10 and C/5. This outcome was attributed to ion transport in the microstructure being the limiting process once there was sufficient carbon coverage to overcome the matrix electronic conductivity resistance in the TNO electrode. Any excess carbon after achieving the electronic conductivity improvement would be expected to further impede ion transport in the interstitial regions between electroactive material particles, and excess carbon can also negatively impact the interfacial resistance of the electroactive materials [8]. The discharge capacities resulting from the full rate capability evaluation of the BF TNO anodes paired with BF LCO cathodes can be found in Supplementary material, Figure S-6.

While the rate capability analysis above reflected the retention of electrochemical capacity, the average discharge voltage was another outcome that changed for the different TNO electrode cells. The average discharge voltage as a function of the discharge C rate for the TNO BF anode cells can be found in Figure 5. At the lowest discharge rate of C/20, all cells had a similar average discharge voltage of 2.17 V. As the C-rates increased, for the 0.0 % sucrose, the average discharge voltage dropped substantially and was 1.64 V at C/5. As the sucrose content increased, the drop in average discharge voltage was mitigated with the 7.5 % sucrose TNO anode cell achieving 1.96 V at C/5.

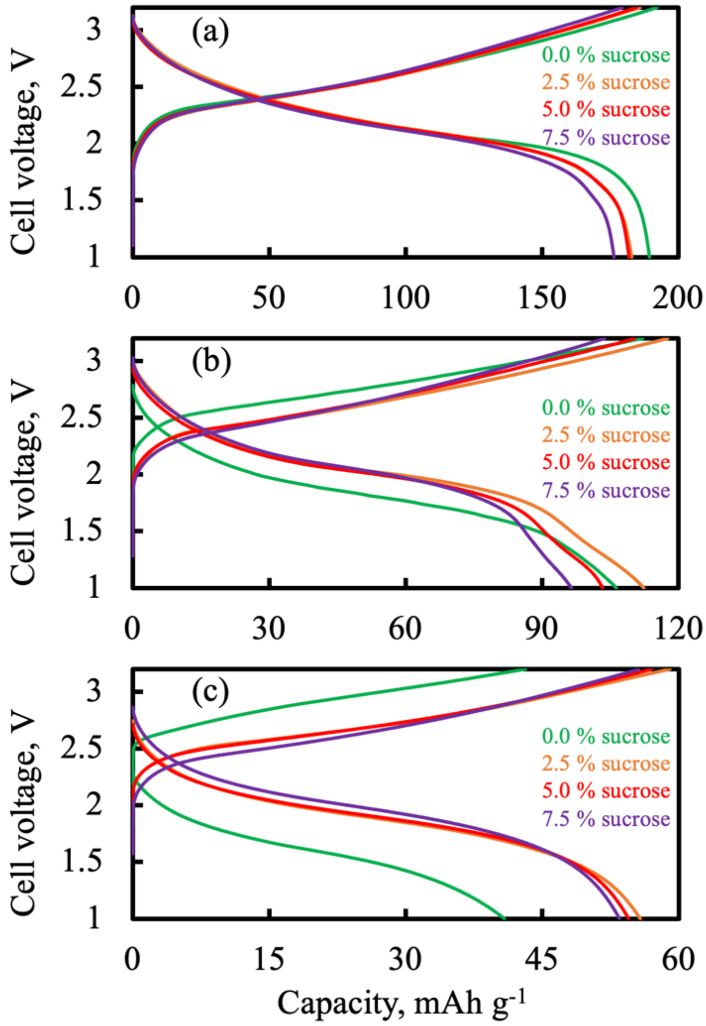

Figure 4. *Voltage profiles of BF electrodes with 0.0 (green), 2.5 (orange), 5.0 (red), and 7.5 % sucrose (purple) in full cells paired with LCO BF cathodes. LCO mass loading was ~1.9 times greater than TNO electrodes to ensure an anode-limited cell. The charge and discharge rates were the same and corresponded to (a) C/20, (b) C/10, and (c) C/5. C/20 corresponded to a current density of 1.7 mA cm^{-2}. All charge and discharge cycles used the same voltage window of 1.0-3.2 V (cell). Note that in the plots, the orange curve generally overlaps with the red and is thus difficult to distinguish*

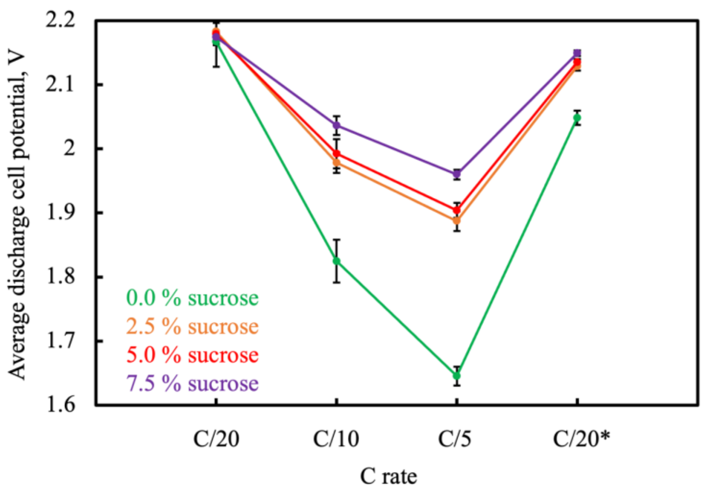

Figure 5. *Average discharge potential of 0.0 (green), 2.5 (orange), 5.0 (red) and 7.5 % sucrose (purple) as the TNO BF cells paired with BF LCO cathodes were cycled at different C rates. All charge and discharge cycles used the same rates, *last five cycles when the charge/discharge rate was reduced back to C/20. C/20 corresponded to ~1.7 mA cm^{-2}*

This outcome suggested the electronic conductivity improvement of the additional carbon helped to increase the average discharge voltage, although the ion transport limitations and Li^+ depletion in the electrolyte likely resulted in the reverse trend for the total capacity at an increasing discharge rate. The average voltage for the last five cycles of the rate capability experiment, where the rate was adjusted back to C/20, also increased as the sucrose content during TNO processing was increased.

ΔdQ/dV peak shift analysis

According to the Butler-Volmer equation [65,66], for most Li-ion battery electroactive materials, the current has an exponential dependence on the overpotential if only considering the interfacial kinetics. Thus, in the ideal case, galvanic charge and discharge of thin composite electrode batteries with low loadings would often primarily reflect the interfacial kinetics at different C rates. dQ/dV plots show the voltage regions corresponding to the delivery of electrochemical capacity. An additional use of dQ/dV is the ΔdQ/dV calculated for shifts in the peak positions between the charge and discharge cycle at the same current density (shift in voltage location of peaks in differential capacity), where the shift is the ΔdQ/dV values as a function of current densities. For batteries with very thick electrodes, such as the BF electrode cells evaluated herein, the overpotential contribution from interfacial compared to ionic and/or electronic overpotential is much smaller, according to previous analysis [7]. For such thick electrodes, the electronic and ionic conductivity of the solid electrode and liquid electrolyte phase can be reflected in the ΔdQ/dV peak position - where the baseline is the dQ/dV peak at low cycling rates, and the ΔdQ/dV is the shift in the peak locations at increasing C rates. For increasing C rates in a cell where the overpotential is primarily due to electronic and/or ionic conductivity through the matrix, it would be expected that the ΔdQ/dV peak positions would shift linearly as a function of increasing current density (or C-rate for identically processed electrodes/cells). Similar analysis was previously reported for indirect evaluation of the impact of the electronic conductivities of BF $LiMn_2O_4$-type (LMO) materials with different dopants and lithiation states [18]. The prior analysis of LMO materials demonstrated that dQ/dV not only serves well to analyze the redox potentials in thin composite electrodes with negligible electronic and ionic overpotentials but also to analyze the electronic and ionic conductivities in thick BF electrodes with relatively low contributions from interfacial overpotentials to the overall cell over-potential [7]. When comparing electroactive materials with different compositions/dopants/treat-ments, using ΔdQ/dV peak positions can exclude the impact of the difference in open circuit voltage (OCV). In addition, with thicker electrodes where lithium depletion, in general, will occur, the peak dQ/dV position well represents the voltage where the electrochemical reactions occur most favorably well before lithium depletion in the cathode region. The Li^+ depletion likely resulted in a more dramatic decrease in voltage, resulting in lower capacity for the TNO BF electrodes with the highest sucrose content during processing.

Plots of the ΔdQ/dV peak positions as a function of areal current densities for all cells with BF TNO anodes can be found in Supplementary material, Figure S-7. As expected for cells with ionic or electronic electrode conductivity being the primary contributors to overpotential, all cells had a linear dependence between the ΔdQ/dV peak positions and current density. As the sucrose content increased, the slope decreased, with these results summarized in Figure 6. In contrast to trans-mission line models or models often assumed in pseudo-two-dimensional simulations [22,65,67], where the current was distributed between the solid electrode and liquid electrolyte across the electrode depth, an overall conductivity (effectively a combination of both electronic conductivity of the electrode and ionic conductivity of electrolyte) can be calculated as in Eq. 1:

$$\sigma = A^{-1}LR^{-1} \tag{1}$$

where σ is the overall conductivity, A is the electrode area, L is the total battery thickness including anode, cathode, and separator, and R is the resistance [68]. Furthermore, we approximate the slope of the $\Delta dQ/dV$ peak position with a unit of V cm^2 mA^{-1} as in Eq. 2:

$$2k = AR \tag{2}$$

where k is the slope. Combining both equations, the approximate overall conductivity can be calculated as in Eq. 3:

$$\sigma = 2k^{-1}L \tag{3}$$

The overall conductivities of all TNO BF anode cells are shown in Figure 6, as the sucrose content increased, the overall conductivity increased and matched the electronic conductivity trend measured for the TNO BF anode pellets. Note that for the 2.5 % sucrose content and higher, the overall conductivity approached and exceeded the ionic conductivity of the electrolyte used, which further supported that the rate capabilities of 2.5 % sucrose and higher sucrose content TNO BF anode cells were not limited by the electronic conductivities of the electrode matrix.

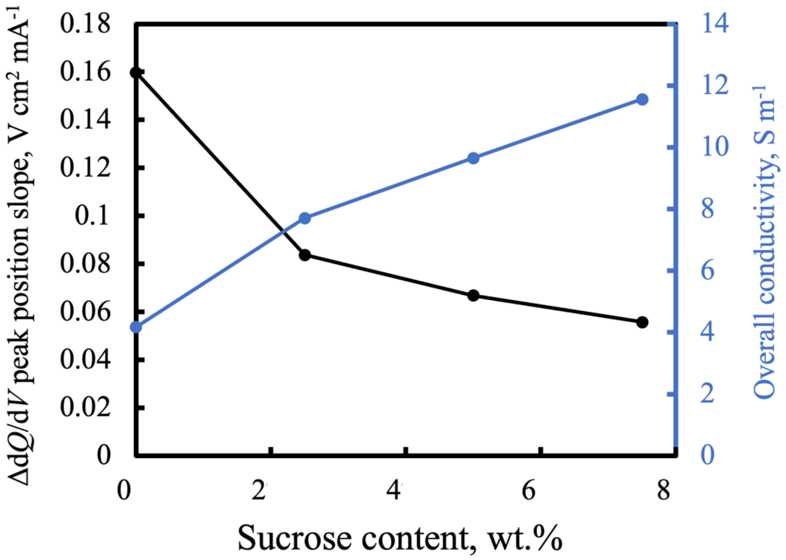

Figure 6. *Slope of ΔdQ/dV peak position (black) and overall conductivity (blue) of BF electrode with 0.0, 2.5, 5.0 and 7.5 % sucrose. Lines added to guide the eye*

Cycle life evaluation was conducted using cells with the relatively thinner BF electrodes at C/2 (2 mA cm^{-2}), and discharge capacity and average discharge voltage can be found in Figure 7. In the first cycle, discharge capacity reached 224, 227, 229, and 235 mAh g^{-1} anode, and average discharge voltages were 2.285, 2.262, 2.296, and 2.302 for 0.0, 2.5, 5.0 and 7.5 % sucrose. The increasing trend in capacity/voltage was consistent with improvements in the electronic conductivity of the TNO material electrode matrix. At the end of 100 cycles, all cells had similar capacity retentions above 60 %. However, the 5.0 % sucrose had the best retention of average discharge voltage, over 70 mV higher than that of 0.0 % sucrose. When examining the Nyquist plots (Figure 8) extracted from EIS on the cells after cycling, the charge transfer resistance of the 5.0 % sucrose was also significantly lower than the 0.0 % sucrose cell. This outcome suggested the carbon coating improved interfacial stability, contributing to improved voltage retention. SEM images of the surfaces of 0.0 % sucrose and 5.0 % sucrose anodes after cycling can be found in Supplementary material, Figure S-8.

Extensive cracks on the electrode are seen on both BF electrodes. Such observation could originate from the large volume change upon cycling for the TNO materials [29,69,70], which supported the similar capacity fade observed among the BF electrodes with varying amounts of carbon coating.

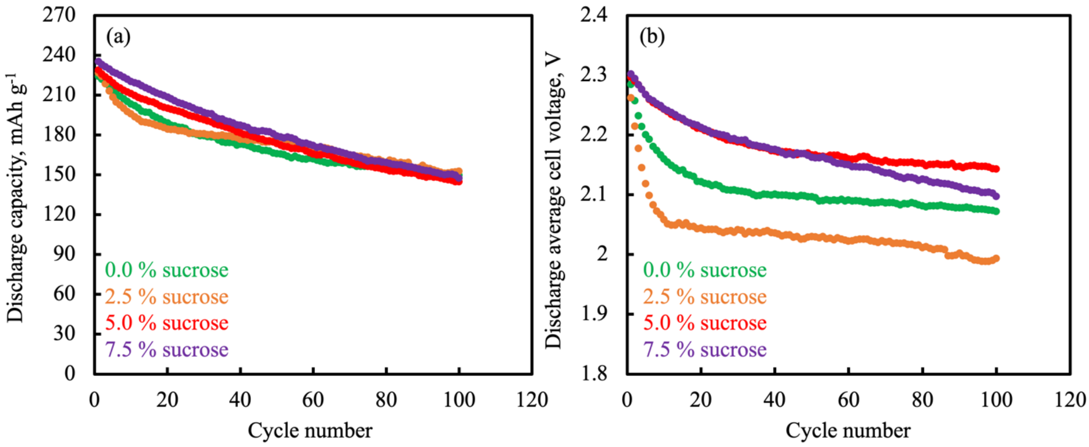

Figure 7. *(a) Discharge capacity and (b) average discharge voltage during cycle life evaluation of cells with thinner BF electrodes for 0.0 % sucrose (green), 2.5 % sucrose (orange), 5.0 % sucrose (red), and 7.5 % sucrose (purple). Charge and discharge cycling was at the same rate of C/2 (2 mA cm^{-2}) within a voltage window of 1-3.2 V (cell)*

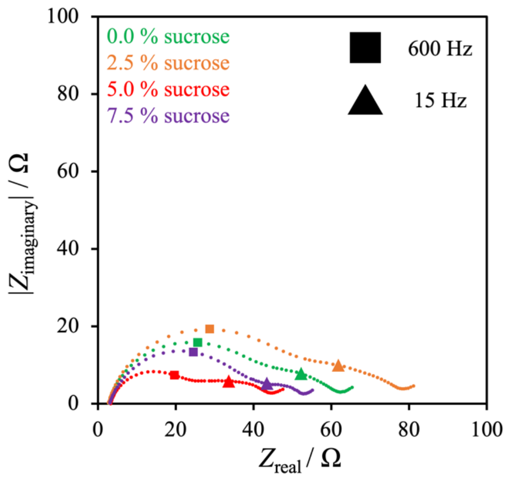

Figure 8. *Nyquist plot extracted from EIS conducted on the thinner BF electrode cells for 0.0 (green), 2.5 (orange), 5.0 (red) and 7.5 % sucrose (purple) at the conclusion of 100 charge/discharge cycles*

Future considerations

The electronic conductivity improvement from carbon coating was beneficial for electrochemical energy storage outcomes for TNO materials, but only up until a certain threshold of carbon added. More generally, many coating materials, including carbon, do not participate in the electrochemical battery reaction and sometimes exacerbate the interfacial kinetics if the coating layer is too thick [71,72]. In a thick electrode architecture, another disadvantage of excess carbon material is that the excess material can potentially take up volume within the electroactive particle interstitial space of the electrode. Additional material within the pore/void volume laden with electrolyte will decrease effective ionic transport properties through the electrode [8,73]. As mentioned earlier, so long as the effective electrode electronic conductivity exceeds approximately 1 S m^{-1}, or roughly the ionic conductivity of the electrolyte ($LiPF_6$ in carbonates) [8,39], the matrix electronic conductivity of the BF electrode no longer limits the capacity of the cell. In the case of higher conductivity electrolytes such as those containing lithium bis(fluorosulfonyl)imide [7,24,74], the threshold for electronic conductivity would be increased to match a value similar in conductivity of the relevant electrolyte.

The carbon coating improved interfacial stability but had little impact on limiting capacity loss during extended cycling. The capacity loss may have been due to volume change during cycling which induced electrode fracturing, which would be consistent with the bulk TNO material properties during lithiation/delithiation. BF electrode particle morphology control and particle encapsulation to mitigate the negative impacts of volume change may provide future opportunities to improve the cycle life of BF electrodes [75-77].

Conclusions

$TiNb_2O_7$ was successfully synthesized using a sol-gel method. Sucrose was incorporated into the processing of the TNO material into porous BF electrodes, where the sucrose played a dual role of the binder during powder processing and carbon source for generating carbon during thermal treatment. As the relative weight fraction of sucrose was increased, the relative amount of carbon in the electrode and the resulting initial measured electrode matrix electronic conductivity also increased. The carbon addition resulted in improvements in rate capability, average discharge voltage, and interfacial stability for cells that used BF anodes containing the TNO materials. This report provides both a robust route for improving electrochemical outcomes when incorporating relatively low electronic conductivity electroactive material in BF electrodes and supports general guidelines for targeting a carbon amount that achieves comparable conductivity to the electrolyte to avoid unnecessary ion transport restrictions from excessive carbon.

Acknowledgement: *This research was funded by the National Science Foundation through grant CBET-1652488.*

References

[1] J. M. Tarascon, M. Armand, Issues and challenges facing rechargeable lithium batteries, *Nature* **414** (2001) 359-367. https://doi.org/10.1038/35104644
[2] M. Pemble, I. Povey, D. Vernardou, Atomic layer deposited V_2O_5 coatings: A promising cathode for li-ion batteries, *Journal of Electrochemical Science and Engineering* **10** (2020) 21-28. https://doi.org/10.5599/jese.708
[3] C. Cai, H. Dong, G. M. Koenig, Anisotropic particle synthesis and characterization for lithium-ion battery electrode materials via precursor precipitate growth inhibitor, *Powder Technology* **394** (2021) 214-224. https://doi.org/10.1016/j.powtec.2021.08.060
[4] H. Dong, G.M. Koenig, Compositional control of precipitate precursors for lithium-ion battery active materials: Role of solution equilibrium and precipitation rate, *Journal of Materials Chemistry A* **5** (2017) 13785-13798. https://doi.org/10.1039/c7ta03653a
[5] M. Ebner, D. W. Chung, R. E. García, V. Wood, Tortuosity anisotropy in lithium-ion battery electrodes, *Advanced Energy Materials* **4** (2014) 1301278. https://doi.org/10.1002/aenm.201301278
[6] K. G. Gallagher, S. E. Trask, C. Bauer, T. Woehrle, S. F. Lux, M. Tschech, P. Lamp, B. J. Polzin, S. Ha, B. Long, Q. Wu, W. Lu, D. W. Dees, A. N. Jansen, Optimizing Areal Capacities through Understanding the Limitations of Lithium-Ion Electrodes, *Journal of The Electrochemical Society* **163** (2016) A138-A149. https://doi.org/10.1149/2.0321602jes
[7] C. Cai, D. Hensley, G. M. Koenig, Simulated discharge overpotential distributions for sintered electrode batteries in rechargeable coin cell form factors, *Journal of Energy Storage* **54** (2022) 105218. https://doi.org/10.1016/j.est.2022.105218
[8] A. Mistry, S. Trask, A. Dunlop, G. Jeka, B. Polzin, P. P. Mukherjee, V. Srinivasan, Quantifying Negative Effects of Carbon-Binder Networks from Electrochemical Performance of Porous Li-Ion Electrodes, *Journal of The Electrochemical Society* **168** (2021) 070536. https://doi.org/10.1149/1945-7111/ac1033

[9] J. Lindberg, H. Lundgren, G. Lindbergh, M. Behm, Benchmarking of electrolyte mass transport in next generation lithium batteries, *Journal of Electrochemical Science and Engineering* **7** (2017) 213-221. https://doi.org/10.5599/jese.408

[10] J. Wu, Z. Ju, X. Zhang, C. Quilty, K. J. Takeuchi, D. C. Bock, A. C. Marschilok, E. S. Takeuchi, G. Yu, Ultrahigh-Capacity and Scalable Architected Battery Electrodes via Tortuosity Modulation, *ACS Nano* **15** (2021) 19109-19118. https://doi.org/10.1021/acsnano.1c06491

[11] M. Armand, P. Axmann, D. Bresser, M. Copley, K. Edström, C. Ekberg, D. Guyomard, B. Lestriez, P. Novák, M. Petranikova, W. Porcher, S. Trabesinger, M. Wohlfahrt-Mehrens, H. Zhang, Lithium-ion batteries - Current state of the art and anticipated developments, *Journal of Power Sources* **479** (2020). https://doi.org/10.1016/j.jpowsour.2020.228708

[12] S. Yan, S. Luo, J. Feng, P. Li, R. Guo, Q. Wang, Y. Zhang, Y. Liu, S. Bao, Rational design of flower-like $FeCo_2S_4$/reduced graphene oxide films: Novel binder-free electrodes with ultra-high conductivity flexible substrate for high-performance all-solid-state pseudocapacitor, *Chemical Engineering Journal* **381** (2020) 122695. https://doi.org/10.1016/j.cej.2019.122695

[13] A. Abouimrane, O. C. Compton, K. Amine, S. T. Nguyen, Non-annealed graphene paper as a binder-free anode for lithium-ion batteries, *Journal of Physical Chemistry C* **114** (2010) 12800-12804. https://doi.org/10.1021/jp103704y

[14] Z. X. Huang, Y. Wang, Y. G. Zhu, Y. Shi, J. I. Wong, H. Y. Yang, 3D graphene supported MoO_2 for high performance binder-free lithium ion battery, *Nanoscale* **6** (2014) 9839-9845. https://doi.org/10.1039/c4nr01744g

[15] R. Elango, A. Nadeina, F. Cadiou, V. Andrade, A. Demortière, M. Morcrette, V. Seznec, Impact of electrode porosity architecture on electrochemical performances of 1 mm-thick $LiFePO_4$ binder-free Li-ion electrodes fabricated by Spark Plasma Sintering, *Journal of Power Sources* **488** (2021) 229402. https://doi.org/10.1016/j.jpowsour.2020.229402

[16] J. Li, T. Zhang, C. Han, H. Li, R. Shi, J. Tong, B. Li, Crystallized lithium titanate nanosheets prepared: Via spark plasma sintering for ultra-high rate lithium ion batteries, *Journal of Materials Chemistry A* **7** (2019) 455-460. https://doi.org/10.1039/c8ta10680k

[17] B. Delattre, R. Amin, J. Sander, J. De Coninck, A. P. Tomsia, Y. M. Chiang, Impact of Pore Tortuosity on Electrode Kinetics in Lithium Battery Electrodes: Study in Directionally Freeze-Cast $LiNi_{0.8}Co_{0.15}Al_{0.05}O_2$(NCA), *Journal of The Electrochemical Society* **165** (2018) A388-A395. https://doi.org/10.1039/c8ta10680k

[18] C. Cai, G. M. Koenig, Investigating Dopants to Improve Sintered $LiMn_2O_4$ Spinel Electrode Electrochemical Cycling Limitations, *Electrochimica Acta* **401** (2021) 139484. https://doi.org/10.1016/j.electacta.2021.139484

[19] J. P. Robinson, J. J. Ruppert, H. Dong, G. M. Koenig, Sintered electrode full cells for high energy density lithium-ion batteries, *Journal of Applied Electrochemistry* **48** (2018) 1297-1304. https://doi.org/10.1007/s10800-018-1242-y

[20] Z. Nie, S. Ong, D. S. Hussey, J. M. Lamanna, D. L. Jacobson, G. M. Koenig, Probing transport limitations in thick sintered battery electrodes with neutron imaging, *Molecular Systems Design and Engineering* **5** (2020) 245-256. https://doi.org/10.1039/c9me00084d

[21] Z. Nie, P. McCormack, H. Z. Bilheux, J. C. Bilheux, J. P. Robinson, J. Nanda, G.M. Koenig, Probing lithiation and delithiation of thick sintered lithium-ion battery electrodes with neutron imaging, *Journal of Power Sources* **419** (2019) 127-136. https://doi.org/10.1016/j.jpowsour.2019.02.075

[22] C. Cai, Z. Nie, J. P. Robinson, D. S. Hussey, J. M. LaManna, D. L. Jacobson, G. M. Koenig, Thick Sintered Electrode Lithium-Ion Battery Discharge Simulations: Incorporating Lithiation-Dependent Electronic Conductivity and Lithiation Gradient Due to Charge Cycle, *Journal of The Electrochemical Society* **167** (2020) 140542. https://doi.org/10.1149/1945-7111/abc747

[23] Z. Nie, R. Parai, C. Cai, C. Michaelis, J. M. LaManna, D. S. Hussey, D. L. Jacobson, D. Ghosh, G. M. Koenig, Pore Microstructure Impacts on Lithium Ion Transport and Rate Capability of Thick Sintered Electrodes, *Journal of The Electrochemical Society* **168** (2021) 060550. https://doi.org/10.1149/1945-7111/ac0bf6

[24] Z. Nie, R. Parai, C. Cai, D. Ghosh, G. M. Koenig, Improving high rate cycling limitations of thick sintered battery electrodes by mitigating molecular transport limitations through modifying electrode microstructure and electrolyte conductivity, *Molecular Systems Design and Engineering* **6** (2021) 708-712. https://doi.org/10.1039/d1me00082a

[25] C. Cai, Z. Nie, G. M. Koenig, Multicomponent two-layered cathode for thick sintered lithium-ion batteries, *Materials Advances* **3** (2022) 4200-4212. https://doi.org/10.1039/d1ma01074c

[26] D. Young, A. Ransil, R. Amin, Z. Li, Y. M. Chiang, Electronic conductivity in the $Li_{4/3}Ti_{5/3}O_4$-$Li_{7/3}Ti_{5/3}O_4$ system and variation with state-of-charge as a Li battery anode, *Advanced Energy Materials* **3** (2013) 1125-1129. https://doi.org/10.1002/aenm.201300134

[27] M. Menetrier, I. Saadoune, S. Levasseur, C. Delmas, The insulator–metal transition upon lithium deintercalation from $LiCoO_2$: electronic properties and ^{7}Li NMR study, *Journal of Materials Chemistry* **9** (1999) 1135-1140. https://doi.org/10.1039/A900016J

[28] S. Levasseur, M. Ménétrier, E. Suard, C. Delmas, Evidence for structural defects in non-stoichiometric HT-$LiCoO_2$: electrochemical, electronic properties and 7Li NMR studies, *Solid State Ionics* **128** (2000) 11-24. https://doi.org/10.1016/S0167-2738(99)00335-5

[29] K. Ise, S. Morimoto, Y. Harada, N. Takami, Large lithium storage in highly crystalline TiNb2O7 nanoparticles synthesized by a hydrothermal method as anodes for lithium-ion batteries, *Solid State Ionics* **320** (2018) 7-15. https://doi.org/10.1016/j.ssi.2018.02.027

[30] D. P. Finegan, A. Quinn, D. S. Wragg, A. M. Colclasure, X. Lu, C. Tan, T. M. M. Heenan, R. Jervis, D. J. L. Brett, S. Das, T. Gao, D. A. Cogswell, M. Z. Bazant, M. Di Michiel, S. Checchia, P. R. Shearing, K. Smith, Spatial dynamics of lithiation and lithium plating during high-rate operation of graphite electrodes, *Energy and Environmental Science* **13** (2020) 2570-2584. https://doi.org/10.1039/d0ee01191f

[31] S. Schweidler, L. De Biasi, A. Schiele, P. Hartmann, T. Brezesinski, J. Janek, Volume Changes of Graphite Anodes Revisited: A Combined Operando X-ray Diffraction and in Situ Pressure Analysis Study, *Journal of Physical Chemistry C* **122** (2018) 8829-8835. https://doi.org/10.1021/acs.jpcc.8b01873

[32] S. Frisco, A. Kumar, J. F. Whitacre, S. Litster, Understanding Li-Ion Battery Anode Degradation and Pore Morphological Changes through Nano-Resolution X-ray Computed Tomography, *Journal of The Electrochemical Society* **163** (2016) A2636-A2640. https://doi.org/10.1149/2.0681613jes

[33] K. J. Griffith, I. D. Seymour, M. A. Hope, M. M. Butala, L. K. Lamontagne, M. B. Preefer, C. P. Koçer, G. Henkelman, A. J. Morris, M. J. Cliffe, S. E. Dutton, C. P. Grey, Ionic and Electronic Conduction in $TiNb_2O_7$, *Journal of the American Chemical Society* **141** (2019) 16706-16725. https://doi.org/10.1021/jacs.9b06669

[34] L. Zhao, S. Wang, Y. Dong, W. Quan, F. Han, Y. Huang, Y. Li, X. Liu, M. Li, Z. Zhang, J. Zhang, Z. Tang, J. Li, Coarse-grained reduced $Mo_xTi_{1-x}Nb_2O_{7+y}$ anodes for high-rate lithium-ion batteries, *Energy Storage Materials* **34** (2021) 574-581. https://doi.org/10.1016/j.ensm.2020.10.016

[35] W. Zhu, B. Zou, C. Zhang, D. H. L. Ng, S. A. El-Khodary, X. Liu, G. Li, J. Qiu, Y. Zhao, S. Yang, J. Lian, H. Li, Oxygen-Defective $TiNb_2O_{7-x}$ Nanochains with Enlarged Lattice Spacing for High-Rate Lithium Ion Capacitor, *Advanced Materials Interfaces* **7** (2020) 2000705. https://doi.org/10.1002/admi.202000705

[36] J. Gao, X. Cheng, S. Lou, Y. Ma, P. Zuo, C. Du, Y. Gao, G. Yin, Self-doping $Ti_{1-x}Nb_{2+x}O_7$ anode material for lithium-ion battery and its electrochemical performance, *Journal of Alloys and Compounds* **728** (2017) 534-540. https://doi.org/10.1016/j.jallcom.2017.09.045
[37] J. T. Han, J. B. Goodenough, 3-V Full Cell Performance of Anode Framework $TiNb_2O_7$/Spinel $LiNi_{0.5}Mn_{1.5}O_4$, *Chemistry of Materials* **23** (2011) 3404-3407. https://doi.org/10.1021/cm201515g
[38] A. A. Voskanyan, K. Jayanthi, A. Navrotsky, Vacancy Control in $TiNb_2O_7$: Implications for Energy Applications, *Chemistry of Materials* **34** (2022) 10311-10319. https://doi.org/10.1021/acs.chemmater.2c01569
[39] A. Nyman, M. Behm, G. Lindbergh, Electrochemical characterisation and modelling of the mass transport phenomena in $LiPF_6$-EC-EMC electrolyte, *Electrochimica Acta* **53** (2008) 6356-6365. https://doi.org/10.1016/j.electacta.2008.04.023
[40] G. M. Koenig, J. Ma, B. Key, J. Fink, K. Bin Low, R. Shahbazian-Yassar, I. Belharouak, Composite of $LiFePO_4$ with titanium phosphate phases as lithium-ion battery electrode material, *Journal of Physical Chemistry C* **117** (2013) 21132-21138. https://doi.org/10.1021/jp4074174
[41] A. Saleem, M. K. Majeed, S. I. Niaz, M. Iqbal, M. Akhlaq, M. Z. Ashfaq, Y. Zhang, H. Gong, Nickel doped copper ferrite $Ni_xCu_{1-x}Fe_2O_4$ for a high crystalline anode material for lithium ion batteries, *New Journal of Chemistry* **45** (2021) 1456-1462. https://doi.org/10.1039/D0NJ04429F
[42] Z. X. Chi, W. Zhang, F. Q. Cheng, J. T. Chen, A. M. Cao, L. J. Wan, Optimizing the carbon coating on LiFePO4 for improved battery performance, *RSC Advances* **4** (2014) 7795-7798. https://doi.org/10.1039/c3ra47702a
[43] D. Gupta, C. Cai, G. M. Koenig, Comparative Analysis of Chemical Redox between Redox Shuttles and a Lithium-Ion Cathode Material via Electrochemical Analysis of Redox Shuttle Conversion, *Journal of The Electrochemical Society* **168** (2021) 050546. https://doi.org/10.1149/1945-7111/ac0068
[44] D. Zuo, C. Wang, G. Tian, K. Shu, X. Liu, Comparative study of Al_2O_3, SiO_2 and TiO_2-coated $LiNi_{0.6}Co_{0.2}Mn_{0.2}O_2$ electrode prepared by hydrolysis coating technology, *Journal of Electrochemical Science and Engineering* **9** (2019) 85-97. https://doi.org/10.5599/jese.624
[45] B. L. Cushing, J. B. Goodenough, Influence of carbon coating on the performance of a $LiMn_{0.5}Ni_{0.5}O_2$ cathode, *Solid State Sciences* **4** (2002) 1487-1493. https://doi.org/10.1016/S1293-2558(02)00044-4
[46] J. T. Han, Y. H. Huang, J. B. Goodenough, New anode framework for rechargeable lithium batteries, *Chemistry of Materials* **23** (2011) 2027-2029. https://doi.org/10.1021/cm200441h
[47] J. Yang, B. Yan, J. Ye, X. Li, Y. Liu, H. You, Carbon-coated $LiCrTiO_4$ electrode material promoting phase transition to reduce asymmetric polarization for lithium-ion batteries, *Physical Chemistry Chemical Physics* **16** (2014) 2882-2891. https://doi.org/10.1039/c3cp54399d
[48] H. Y. Lee, J. K. Baek, S. W. Jang, S. M. Lee, S. T. Hong, K. Y. Lee, M. H. Kim, Characteristics of carbon-coated graphite prepared from mixture of graphite and polyvinylchloride as anode materials for lithium ion batteries, *Journal of Power Sources* **101** (2001) 206-212. https://doi.org/10.1016/S0378-7753(01)00671-1
[49] T. Yang, N. Zhang, Y. Lang, K. Sun, Enhanced rate performance of carbon-coated $LiNi_{0.5}Mn_{1.5}O_4$ cathode material for lithium ion batteries, *Electrochimica Acta* **56** (2011) 4058-4064. https://doi.org/10.1016/j.electacta.2010.12.109
[50] V. Pavitra, I. Soni, B. M. Praveen, G. Nagaraju, Brief review on carbon derivatives based ternary metal oxide composite electrode materials for lithium-ion batteries, *Journal of Electrochemical Science and Engineering* **14(3)** (2023) 605-640. https://doi.org/10.5599/jese.1470

[51] R. Parai, N. B. Gundrati, S. Akurati, G. M. Koenig, D. Ghosh, Microstructure in the transition region and steady-state region of ice-templated sintered lithium titanate $Li_4Ti_5O_{12}$ materials fabricated with and without sucrose, *Journal of Materials Research* **36** (2021) 3519-3538. https://doi.org/10.1557/s43578-021-00367-3

[52] L. Perfler, V. Kahlenberg, C. Wikete, D. Schmidmair, M. Tribus, R. Kaindl, Nanoindentation, High-Temperature Behavior, and Crystallographic/Spectroscopic Characterization of the High-Refractive-Index Materials $TiTa_2O_7$ and $TiNb_2O_7$, *Inorganic Chemistry* **54** (2015) 6836-6848. https://doi.org/10.1021/acs.inorgchem.5b00733

[53] R. Tao, G. Yang, E. C. Self, J. Liang, J. R. Dunlap, S. Men, C. L. L. Do-Thanh, J. Liu, Y. Zhang, S. Zhao, H. Lyu, A. P. Sokolov, J. Nanda, X. G. G. Sun, S. Dai, Ionic Liquid-Directed Nanoporous $TiNb_2O_7$ Anodes with Superior Performance for Fast-Rechargeable Lithium-Ion Batteries, *Small* **16** (2020) 2001884. https://doi.org/10.1002/smll.202001884

[54] R. Qian, H. Lu, T. Yao, F. Xiao, J. W. Shi, Y. Cheng, H. Wang, Hollow $TiNb_2O_7$ Nanospheres with a Carbon Coating as High-Efficiency Anode Materials for Lithium-Ion Batteries, *ACS Sustainable Chemistry and Engineering* **10** (2022) 61-70. https://doi.org/10.1021/acssuschemeng.1c04712

[55] W. Chung, J. H. Bang, Carbon-Doped $TiNb_2O_7$ Suppresses Amorphization-Induced Capacity Fading, *ACS Applied Materials and Interfaces* **14** (2022) 19365-19375. https://doi.org/10.1021/acsami.2c00589

[56] Y. Zhang, Y. Tang, L. Liu, Y. Gao, C. Zhu, X. Bai, X. Wang, $TiNb_xO_{2+2.5x}$ (x=2, 5, 6)/C hybrid nanotubes with enhanced kinetics for high-performance lithium anodes, *Electrochimica Acta* **410** (2022) 139862. https://doi.org/10.1016/j.electacta.2022.139862

[57] L. Hu, L. Luo, L. Tang, C. Lin, R. Li, Y. Chen, $Ti_2Nb_{2x}O_{4+5x}$ anode materials for lithium-ion batteries: A comprehensive review, *Journal of Materials Chemistry A* **6** (2018) 9799-9815. https://doi.org/10.1039/c8ta00895g

[58] X. Bin Zhong, T. T. Huang, J. F. Liang, S. X. Li, H. H. Zhang, G. Y. Liu, G. M. Wang, Porous $TiNb_2O_7$@N-C as anode materials for lithium-ion batteries with ultrahigh-rate performance, *Journal of Physical Chemistry C* **125** (2021) 23960-23967. https://doi.org/10.1021/acs.jpcc.1c07463

[59] D. A. Khoviv, S. V. Zaytsev, V. M. Ievlev, Electronic structure and formation mechanism of complex Ti-Nb oxide, *Thin Solid Films* **520** (2012) 4797-4799. https://doi.org/10.1016/j.tsf.2011.10.130

[60] J. Lee, H. H. Kwak, S. E. Bak, G. J. Lee, S. T. Hong, M. A. Abbas, J. H. Bang, New Class of Titanium Niobium Oxide for a Li-Ion Host: $TiNbO_4$ with Purely Single-Phase Lithium Intercalation, *Chemistry of Materials* **34** (2022) 854-863. https://doi.org/10.1021/acs.chemmater.1c03960

[61] C. I. Thomas, M. Karppinen, Intercalation of Primary Alcohols into Layered Titanoniobates, *Inorganic Chemistry* **56** (2017) 9132-9138. https://doi.org/10.1021/acs.inorgchem.7b01135

[62] C. Yang, S. Deng, C. Lin, S. Lin, Y. Chen, J. Li, H. Wu, Porous $TiNb_{24}O_{62}$ microspheres as high-performance anode materials for lithium-ion batteries of electric vehicles, *Nanoscale* **8** (2016) 18792-18799. https://doi.org/10.1039/c6nr04992c

[63] C. Lin, S. Deng, D. J. Kautz, Z. Xu, T. Liu, J. Li, N. Wang, F. Lin, Intercalating $Ti_2Nb_{14}O_{39}$ Anode Materials for Fast-Charging, High-Capacity and Safe Lithium-Ion Batteries, *Small* **13** (2017) 1702903. https://doi.org/10.1002/smll.201702903

[64] X. Wu, J. Miao, W. Han, Y. S. Hu, D. Chen, J. S. Lee, J. Kim, L. Chen, Investigation on $Ti_2Nb_{10}O_{29}$ anode material for lithium-ion batteries, *Electrochemistry Communications* **25** (2012) 39-42. https://doi.org/10.1016/j.elecom.2012.09.015

[65] T. F. Fuller, M. Doyle, J. Newman, Simulation and Optimization of the Dual Lithium Ion Insertion Cell, *Journal of The Electrochemical Society* **141** (1994) 1. https://doi.org/10.1149/1.2054684

[66] E. Martínez-Rosas, R. Vasquez-Medrano, A. Flores-Tlacuahuac, Modeling and simulation of lithium-ion batteries, *Computers and Chemical Engineering* **35** (2011) 1937-1948. https://doi.org/10.1016/j.compchemeng.2011.05.007
[67] R. Morasch, J. Keilhofer, H. A. Gasteiger, B. Suthar, Methods—Understanding Porous Electrode Impedance and the Implications for the Impedance Analysis of Li-Ion Battery Electrodes, *Journal of The Electrochemical Society* **168** (2021) 080519. https://doi.org/10.1149/1945-7111/ac1892
[68] I. V. Thorat, D. E. Stephenson, N. A. Zacharias, K. Zaghib, J. N. Harb, D. R. Wheeler, Quantifying tortuosity in porous Li-ion battery materials, *Journal of Power Sources* **188** (2009) 592-600. https://doi.org/10.1016/j.jpowsour.2008.12.032
[69] C. Cai, G.M. Koenig, Processing Temperature Impact on $TiNb_2O_7$ Thick All Active Material Lithium-Ion Battery Electrodes, *Journal of The Electrochemical Society* **170** (2023) 10529. https://doi.org/10.1149/1945-7111/acb403
[70] B. Guo, X. Yu, X. G. Sun, M. Chi, Z. A. Qiao, J. Liu, Y. S. Hu, X. Q. Yang, J. B. Goodenough, S. Dai, A long-life lithium-ion battery with a highly porous $TiNb_2O_7$ anode for large-scale electrical energy storage, *Energy and Environmental Science* **7** (2014) 2220-2226. https://doi.org/10.1039/c4ee00508b
[71] Y. Da Cho, G. T. K. Fey, H. M. Kao, The effect of carbon coating thickness on the capacity of $LiFePO_4$/C composite cathodes, *Journal of Power Sources* **189** (2009) 256-262. https://doi.org/10.1016/j.jpowsour.2008.09.053
[72] J. Wang, X. M. Liu, H. Yang, X. D. Shen, Characterization and electrochemical properties of carbon-coated $Li_4Ti_5O_{12}$ prepared by a citric acid sol-gel method, *Journal of Alloys and Compounds* **509** (2011) 712-718. https://doi.org/10.1016/j.jallcom.2010.07.215
[73] A. N. Mistry, K. Smith, P. P. Mukherjee, Secondary-Phase Stochastics in Lithium-Ion Battery Electrodes, *ACS Applied Materials and Interfaces* **10** (2018) 6317-6326. https://doi.org/10.1021/acsami.7b17771
[74] S. D. Han, O. Borodin, D. M. Seo, Z. B. Zhou, W. A. Henderson, Electrolyte Solvation and Ionic Association, *Journal of The Electrochemical Society* **161** (2014) A2042-A2053. https://doi.org/10.1149/2.0101414jes
[75] M. Lin, D. Cheng, J. Liu, L. Ouyang, R. Hu, J. Liu, L. Yang, M. Zhu, Dual-Carbon-Confined SnS Nanostructure with High Capacity and Long Cycle Life for Lithium-ion Batteries, *Energy & Environmental Materials* **4** (2021) 562-568. https://doi.org/10.1002/eem2.12136
[76] A. M. Bruck, C. A. Cama, C. N. Gannett, A. C. Marschilok, E. S. Takeuchi, K. J. Takeuchi, Nano-crystalline iron oxide based electroactive materials in lithium ion batteries: the critical role of crystallite size, morphology, and electrode heterostructure on battery relevant electroche-mistry, *Inorganic Chemistry Frontiers* **3** (2016) 26-40. https://doi.org/10.1039/C5QI00247H
[77] Y. Park, N. S. Choi, S. Park, S. H. Woo, S. Sim, B. Y. Jang, S. M. Oh, S. Park, J. Cho, K. T. Lee, Si-Encapsulating Hollow Carbon Electrodes via Electroless Etching for Lithium-Ion Batteries, *Advanced Energy Materials* **3** (2013) 206-212. https://doi.org/10.1002/aenm.201200389